AIAA Aviation
16-20 June 2014, Atlanta, GA
20th AIAA/CEAS Aeroacoustics Conference

An experimental characterisation of wall pressure wavevector-frequency spectra in the presence of pressure gradients

Édouard Salze[1], Christophe Bailly[2], Olivier Marsden[3], Emmanuel Jondeau[4], and Daniel Juvé[5]

Laboratoire de Mécanique des Fluides et d'Acoustique,
École Centrale de Lyon & UMR CNRS 5509, 69134 Écully, France

The goal of this experimental study is to investigate the wall pressure wavenumber-frequency spectra induced by a turbulent boundary layer in the presence of a mean pressure gradient. The mean pressure gradient is achieved by changing the ceiling angle of a rectangular channel flow. Wall pressure spectra are measured for zero-, adverse- and favorable-pressure-gradient boundary layers by using a pinhole microphone in conjunction with a high-frequency-calibration procedure. A linear antenna based on a non-uniform distribution of remote microphones mounted on a rotating disk is also developed to obtain a direct measurement of both aerodynamic and acoustic components of wavenumber-frequency spectra. First results, comparisons and analyses are then discussed.

Nomenclature

C_p	pressure coefficient
h	height of the channel
$H = \delta_1/\delta_\theta$	shape factor
$\boldsymbol{k}$	wavevector ($\boldsymbol{k} \in \mathbf{R}^3$)
p_w	wall pressure
$q_0 = \rho U_0^2/2$	dynamic pressure
$\mathrm{Re}_{\delta_1} = U_\infty \delta_1/\nu$	Reynolds number based on δ_1
$\mathrm{Re}^+ = u_\tau \delta/\nu$	Kármán or friction Reynolds number
$\boldsymbol{r}$	separation vector (polar coordinates)
$R_{pp}(\boldsymbol{r}, \omega)$	pressure cross spectral density
$S_{pp}(\omega) = R_{pp}(\boldsymbol{r} = 0, \omega)$	one-sided wall pressure spectrum

[1] Post-doctoral fellow.
[2] Professor, corresponding author, e-mail: christophe.bailly@ec-lyon.fr, AIAA senior member.
[3] Assistant professor.
[4] Engineer.
[5] Professor.

U_0	inlet velocity (at $x_1 = 0$)
U_∞	local free-stream velocity at $x_{1\text{ref}}$
U_c	convection velocity
u_τ	friction velocity
$\boldsymbol{x} = (x_1, x_2, x_3)$	Cartesian coordinates, see Fig. 1
$\beta = (\delta_1/\tau_w) dP_e/dx_1$	Clauser parameter
δ	boundary layer thickness
δ_1	boundary layer displacement thickness
δ_θ	boundary layer momentum thickness
$\gamma(\boldsymbol{\xi}, \omega)$	coherence function, see Eq. (9)
ν	kinetic viscosity
$\omega = 2\pi f$	angular frequency ($\omega \geq 0$)
$\omega_{\delta_1} = \omega\delta_1/U_\infty$	dimensionless angular frequency
$\Phi_{pp}(\boldsymbol{k}, \omega)$	wavevector-frequency wall pressure spectrum
ρ	density
$\tau_w = \rho u_\tau^2$	wall shear stress
$\boldsymbol{\xi}$	separation vector

The superscript $+$ denotes a dimensionless quantity using viscous scaling, e.g. $x_3^+ = x_3 u_\tau/\nu$.

I. Introduction

The understanding of vibrations and noise induced by wall pressure fluctuations is of importance in hydroacoustics [4, 48], but also in aeronautical [28, 52] and more recently in automotive applications [5, 6, 34]. The motivations behind the present experimental investigation are twofold. First, a direct measurement of the wall pressure wavevector-frequency spectrum induced by a turbulent boundary layer, including both aerodynamic and acoustic components of loading is desirable. The aerodynamic part is associated with the indirect contribution to cabin noise through panel vibration while the acoustic part represents a direct contribution to this noise. Despite the fact that this is in principle a non-intrusive measurement, the small separation distance between sensors and the large dynamic range between the two components make this experimental characterisation quite tricky [2, 19, 22]. Mainly the incompressible part of spectra has been reported over the past fifty years [8, 33]. It must be also mentioned that these difficulties are also encountered in numerical simulations [24, 30, 32]. Second, zero-pressure-gradient turbulent boundary layers are often considered. Only a fragmented view is currently offered regarding pressure gradient effects, even for modelling the aerodynamic loading [10, 36, 46].

In a previous study by Arguillat *et al.* [2], a rotating microphone array was used to estimate both the aerodynamic and the acoustic part of the wall pressure wavevector-frequency spectrum through an original post-processing. Results have been reported for a turbulent boundary layer at a Reynolds number $\text{Re}_{\delta_\theta} = u_\tau\delta_\theta/\nu = 1716$ and at a moderate velocity $U_\infty = 44$ m.s^{-1} and the feasibility of obtaining pressure spectra by this original approach was demonstrated.

In these expressions, u_τ denotes the friction velocity, δ_θ the momentum thickness and U_∞ the free stream velocity of the boundary layer, and ν is the kinematic viscosity of the fluid. It was also noticed that some improvements could be carried out in the future regarding the test channel as well as the antenna.

In the present work, wall pressure fluctuations induced by a turbulent flow are investigated and the experimental approach is revisited and significantly improved in order to better access wavevector-frequency spectra beneath a boundary layer. A new channel is used for flow-acoustic measurements. The ceiling of the test section can be inclined, which allows turbulent boundary layers in the presence of pressure gradients to be considered. A new disk antenna, mounted on a rigid flat plate, is also developed and carefully manufactured, to allow the determination of wall pressure wavevector-frequency spectra.

The present paper is organized as follows. The experimental setup is described in Section II as well as some results regarding the characterisation of the turbulent boundary layer. The new microphone disk antenna is presented in Section III. Pressure spectra measured through a pinhole microphone are reported and discussed in Section IV A, and wavevector-frequency spectra are studied in Section IV C. Concluding remarks are given in Section V. The calibration procedure is explained in Appendix A and additional details are also provided in Appendix B.

II. Experimental setup

The experiments were conducted in the main subsonic wind tunnel of the Centre Acoustique at Ecole Centrale de Lyon in France [2, 40]. The flow is generated by a 350 kW Neu centrifugal blower delivering a nominal mass flow rate of 15 kg.s^{-1}, and the fan is powered by an electronically controlled Tridge-Electric LAK 4280A motor. Air passes through a settling chamber including a honeycomb and several wire meshes designed to reduce free stream turbulence. Acoustic treatment on the wind tunnel walls and baffled silencers allows to reduce the noise level and to prevent contamination of acoustic measurements performed in the anechoic chamber. This results in an air flow at ambient temperature with a low background noise and low residual turbulence intensity, less than 1%.

A sketch of the channel is shown in Fig. 1. As mentioned in the introduction, the two parts of the ceiling can be sloped to control the mean pressure gradient inside the channel [38], and to impose a particular value at $x_{1\text{ref}} = 3h$, where h is the channel height. Three configurations have been retained in the present study, corresponding to a turbulent boundary layer submitted to a zero-pressure-gradient (zpg), a favorable or negative pressure gradient (fpg) and an adverse or positive pressure gradient (apg). The geometrical parameters are provided in Table 2. The side walls of the second part of the channel have been acoustically treated using a wire mesh and a porous liner, in order to reduce noise generated by the jet at the channel outlet. Other choices are possible, as in Monty *et al.* [37] for instance, but it should be noted here that achieving channel airtightness is quite challenging for high flow speeds $U_0 \simeq 100$ m.s^{-1}. A picture of the test channel is reproduced in Fig. 6.

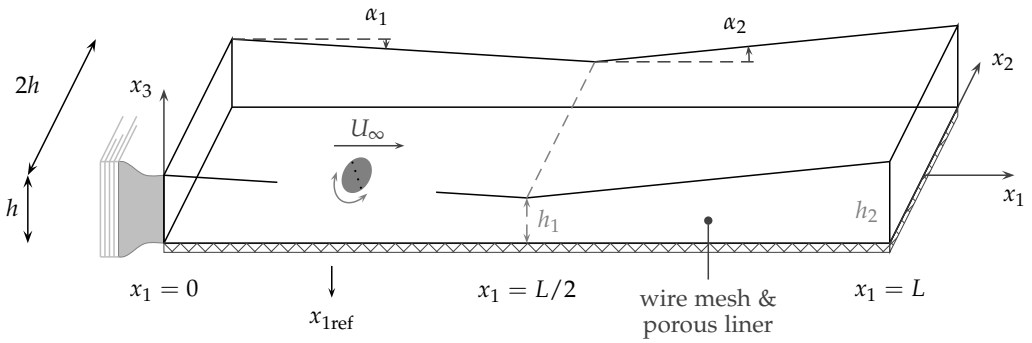

Fig. 1 Sketch of the test channel and notations. The height of the initial section is $h = 250$ mm, the length of the whole channel is $L = 16h$ and the location of the disk antenna is $x_{\text{ref}} = 3h$. It should be noted that U_0 is the velocity at the channel inlet ($x_1 = 0$), and that U_∞ is the local free stream velocity of the boundary layer at the streamwise location of the measurement, $x_{1\text{ref}}$ for the rotating antenna.

configuration	α_1	α_2	h_1 (cm)	h_2 (cm)	$U_0\|_{\text{max}}$
zpg-BL	0.3°	3.9°	26.5	40	100 m.s^{-1}
fpg-BL	−3.5°	1.5°	12.75	18	50 m.s^{-1}
apg-BL	4°	4°	39	51	100 m.s^{-1}

Table 2 Geometrical parameters of the three configurations considered in this study, refer to Fig. 1 for the notations.

The boundary layer thickness is always very small with respect to the channel height h. Therefore, independent boundary layers develop on the walls. Homogeneity of the mean flow in the spanwise direction was checked. The floor contains three plug rows at $x_2 = 0$ and $x_2 = \pm 0.6h$ to measure the mean pressure distribution $\bar{p}$ along x_1, and the mean flow was found to be homogeneous in the middle part of the channel. The mean static pressure $\bar{p}$ has been measured using a Validyne dp15 transducer. The evolution of the pressure coefficient gradient along the channel centerline $x_2 = 0$ is shown in Fig. 2 for the two configurations apg and fpg, and for different velocities. The pressure coefficient is defined as $C_p = (\bar{p} - p_{\text{amb}})/q_0$ where q_0 is the dynamic pressure at the channel inlet. Each point considered in the present study is denoted by a configuration, namely zpg or apg or fpg, which is associated to the three positions of the channel ceiling given in Table 2, and by a number associated to the free stream velocity U_∞ at $x_{1\text{ref}}$. Experimental parameters are provided in Table 3. The evolution of the pressure gradient can be well represented [17] by the following expression

$$\frac{dC_p}{dx_1} = -\frac{2L_0^2}{(L_0 - x_1)^3} \tag{1}$$

where L_0 is not exactly equal to the physical length of the channel due to installation effects. It is found that $L_0 = -14h$ for the apg configuration, and $L_0 = 14.8h$ for the fpg configu-

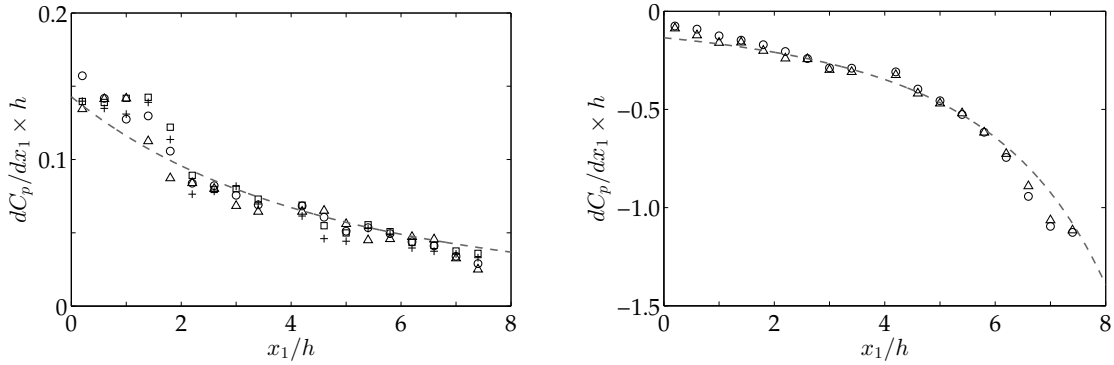

Fig. 2 Longitudinal profile of the normalized mean pressure gradient $C_p/dx_1 \times h$ as a function of the dimensionless distance x_1/h. On the left, for △ apg19, ○ apg38, ◊ apg57, + apg76 and on the right for △ fpg32, ○ fpg63. The semi-empirical law (1) is also shown in dashed gray line.

	U_∞	$\delta_1 \times 10^3$	H	u_τ	Re_{δ_1}	Re^+	β
zpg	11	3.1	1.34	0.48	2.2×10^3	633	–
	25	2.8	1.30	1.02	4.7×10^3	1006	–
	36	3.2	1.30	1.35	7.4×10^3	1778	–
	45	3.7	1.31	1.65	1.1×10^4	2718	–
	59	3.6	1.31	2.05	1.4×10^4	3374	–
	76	2.9	1.28	2.71	1.5×10^4	3559	–
	100	3.5	1.30	3.54	2.3×10^4	5050	–
apg	8	8.4	1.38	0.31	4.6×10^3	1036	0.95
	12	8.2	1.42	0.42	6.7×10^3	1122	1.06
	19	6.2	1.41	0.66	7.9×10^3	1321	0.83
	27	5.0	1.36	0.96	9.1×10^3	1596	0.64
	38	5.5	1.31	1.34	1.4×10^4	3555	0.71
	45	5.8	1.31	1.55	1.8×10^4	5135	0.81
	57	5.2	1.31	1.95	2.0×10^4	5139	0.72
	76	6.0	1.31	2.45	3.0×10^4	8027	0.94
fpg	10	2.1	1.27	0.50	1.5×10^3	501	−0.48
	32	2.1	1.24	1.35	4.6×10^3	1353	−0.63
	45	1.7	1.23	1.90	5.0×10^3	1881	−0.50
	63	1.8	1.22	2.53	7.5×10^3	2490	−0.59

Table 3 Boundary layer parameters for the present experiments at ECL.

ration. The streamwise evolution of the derivative of the pressure coefficient is found to be independent of the velocity as expected.

Velocity profiles have been measured with a Dantec 55P01 hot-wire operating in constant voltage mode using a Streamline anemometer. The homogeneity of the mean flow in the

spanwise direction was checked, and the longitudinal evolution of the boundary layer was also investigated. Velocity profiles are usually normalised with the friction velocity u_τ to get dimensionless results and exhibit scaling laws. Although the skin friction coefficient $C_f = 2(u_\tau/U_\infty)^2$ can independently be measured in particular cases, this velocity is most often indirectly estimated. The Clauser method [11] is mainly used in this work since velocity profiles include a logarithmic region [51] and the possible mean pressure gradients remain moderate [37]. In a preliminary stage of the present work, the friction velocity was however estimated from the Gruschwitz's momentum integral equation (see Schlichting [45], chap. VIII, Eq. 8.32)

$$u_\tau^2 = \frac{d}{dx_1}(U_\infty^2 \delta_\theta) - \frac{1}{\rho}\frac{d\bar{p}}{dx_1}\delta_1$$

which reduces to $C_f = 2d\delta_\theta/dx_1$ for a zero-pressure-gradient boundary layer. The streamwise evolution of the momentum thickness must be accurately known for this approach to be used. Moreover, a hot-film flush-mounted probe (Dantec 55R47) has also been implemented on the channel floor. The three estimations of the friction velocity have been found in good agreement. Finally, note that all the velocity profiles are located at $x_{1\text{ref}}$ in what follows.

Mean velocity profiles measured in the zpg configuration are displayed in Fig. 3 (left) using wall variables. They are chosen thanks to the shape factor $H \simeq 1.30 - 1.31$ and for increasing Reynolds numbers Re^+ in Table 3. The logarithmic law is also plotted in dashed gray line. Using inner variables, all the profiles collapse in a single curve near the wall and in the logarithmic region. The disparity between inner and outer length scales is also clearly visible near the edge of the boundary layer as the Reynolds $\mathrm{Re}^+ = \delta/(\nu/u_\tau)$ increases. A frequency spectrum of the longitudinal velocity fluctuation u_1' is shown in Fig. 3 (right) at $x_3^+ \simeq 109$ for the zpg45 case, for which $u_1'/U_\infty = 0.09$. The -1 and $-5/3$ power laws are also plotted in gray dashed lines. The signal has been recorded over a large period to correctly resolve the low frequency part of this one-dimensional spectrum. For the zpg45 case, the length of the probe is $l_{\text{hwa}}^+ \simeq 136$ using a viscous scaling. Therefore, smallest scales of the flow cannot be correctly measured. Using Taylor's assumption, the cut-off frequency is estimated to be $\omega\delta_1/U_\infty|_{\max} \simeq 11$, in agreement with the plotted spectrum. The $-5/3$ power law is indeed well retrieved up to this frequency.

Some mean velocity profiles are also displayed in Fig. 4 in the presence of a mean pressure gradient. Again, the logarithmic law is also superimposed in grey dashed line using the same values for the constants. Overall all the curves collapse near the wall and in the overlaped region. Near the free edge of the boundary layer, adverse and favorable mean pressure gradients induce opposite effects for the wake law of velocity profiles. The importance of this deficit law can be evaluated through the wake parameter Π introduced by Coles [12], defined from the following expression

$$\overline{U}_1^+(x_3^+) = \frac{1}{\kappa}\log(x_3^+) + B + \frac{2\Pi}{\kappa} w\left(\frac{x_3}{\delta}\right)$$

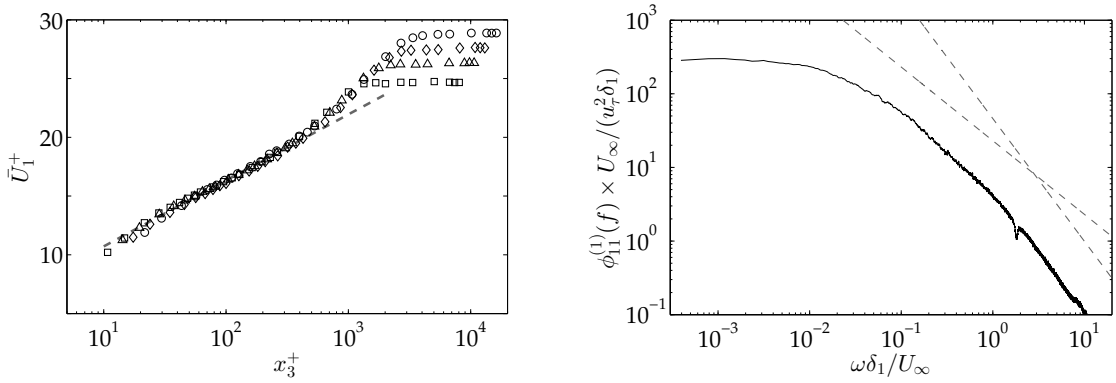

Fig. 3 On the left, mean velocity profiles measured at $x_{1\mathrm{ref}}$ in the zpg configuration: □ zpg25, △ zpg36, ◊ zpg45 and ○ zpg59, refer to Table 3. The logarithmic law $\overline{U}_1^+ = (1/\kappa)\log(x_3^+) + B$ with $\kappa = 0.41$ and $B = 5.1$ is displayed in grey dashed line. On the right, one-sided frequency spectrum $\phi_{11}^{(1)}(f)$ of the longitudinal velocity fluctuation u_1' measured at $x_3^+ \simeq 109$ by hot wire anemometer with a sampling frequency $f_s = 102.4$ kHz over a period $T = 90$ s. The -1 and -5/3 power laws are indicated in grey dashed lines.

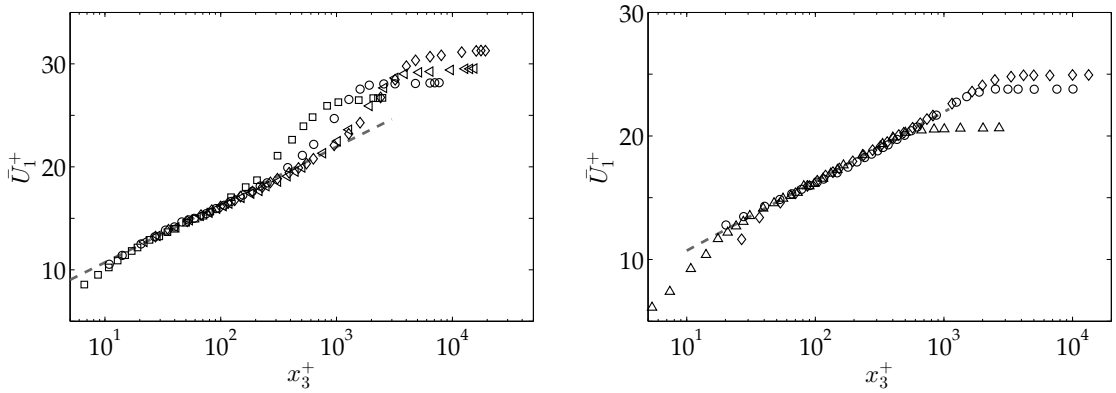

Fig. 4 Mean velocity profiles measured at $x_{1\mathrm{ref}}$ in the presence of a mean pressure gradient. On the left, in the apg configuration: △ apg8, ○ apg27, ◊ apg57, □ apg76. On the right, in the fpg configuration: △ fpg10, ○ fpg45, ◊ fpg63. The logarithmic law (see caption of Fig. 3) is displayed in grey dashed line.

with $w(1) = 2$. Its value increases with the Reynolds number [9], and also increases with $\beta > 0$ and strongly decreases for the fpg configuration. This can be also clearly identified by examining the fluctuating velocity profiles, not shown here to save space, and turbulence intensity increases as β increases for similar friction Reynolds numbers in the apg configuration, and decreases in the fpg configuration.

Pressure gradient effects on the boundary layer development have been studied for a long time, but it remains quite tricky to investigate the influence of a single parameter. As an illustration, the zpg45 and apg8 points have a similar Reynolds number $\mathrm{Re}^+ \simeq 1000$, and also the zpg76

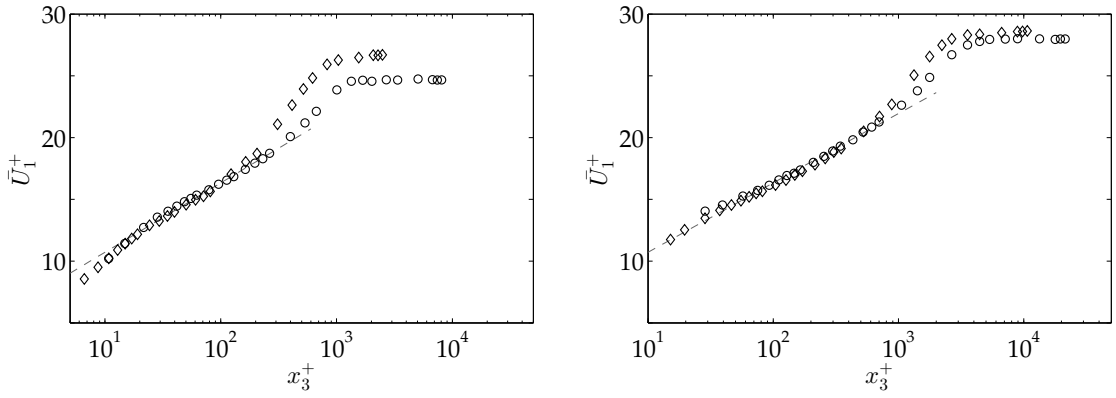

Fig. 5 Comparison between zpg and apg mean flow profiles at similar friction Reynolds numbers. Left, $Re^+ \simeq 1000$, ∘ zpg25 and ◊ apg8 ($\beta = 0.95$). Right, $Re^+ \simeq 3560$, ∘ zpg76 and ◊ apg38 ($\beta = 0.71$). – – – logarithmic law.

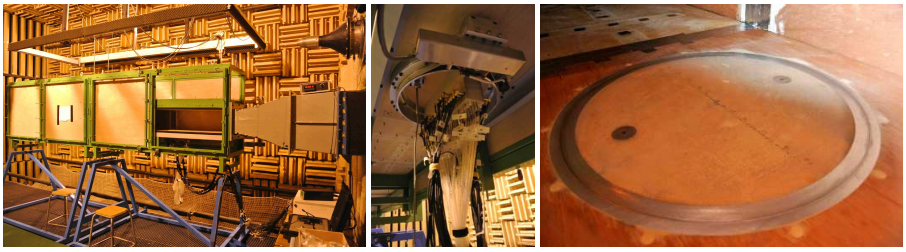

Fig. 6 From the left to the right, whole view of the channel flow, rear view of the rotating disk and view of the pressure antenna on the front side of this disk.

and apg38 with $Re^+ \simeq 3560$, from Table 3. Note however that the shape factor is never the same. These velocity profiles are shown in Fig. 5 to highlight the influence of β, in particular in the free edge of the boundary layer. The wake parameter is found to be $\Pi \simeq 0.28$ and 0.48 for the case $Re^+ \simeq 1000$, but $\Pi \simeq 0.40$ and 0.37 for the case $Re^+ \simeq 3560$.

III. Rotating microphone antenna

Pressure signals are recorded using 63 remote microphone probes and a pinhole microphone. Further details about the design of the pressure antenna can be found in section III.B. Pressure signals are simultaneously recorded over the 63 probes at a sampling frequency of 51.2 kHz. Pictures of the pressure antenna have been reproduced in Fig. 6. The front side of the pressure antenna on the rotating disk is visible on the left, and the rear side of the pressure antenna is visible on the right. Signal processing is discussed in section III.A.

A. Basic signal processing

A brief overview of the signal processing is first presented. The Fourier transform $\hat{p}(\boldsymbol{k},\omega)$ of the pressure field $p(\boldsymbol{x},t)$ in space and in time is defined by

$$p(\boldsymbol{x},t) = \iint \hat{p}(\boldsymbol{k},\omega) e^{i(\boldsymbol{k}\cdot\boldsymbol{x}-\omega t)} d\boldsymbol{k} d\omega = \mathcal{F}^{-1}\left\{\hat{p}(\boldsymbol{k},\omega)\right\}$$

Assuming stationary random signals and ergodicity, the cross spectral density is defined as,

$$R_{pp}(\boldsymbol{x},\boldsymbol{r},\omega) = \lim_{T\to\infty} \frac{2\pi}{T} E\left[\hat{p}(\boldsymbol{x},\omega)\hat{p}^{\star}(\boldsymbol{x}+\boldsymbol{r},\omega)\right]$$

where $\boldsymbol{r}$ is the separation vector between two probes located at $\boldsymbol{x}$ and $\boldsymbol{x}+\boldsymbol{r}$. In practice, the wall pressure field is assumed to be homogeneous over the microphone array, that is, $R_{pp}(\boldsymbol{x},\boldsymbol{r},\omega) = R_{pp}(\boldsymbol{r},\omega)$. The Welch method is applied by splitting the time signal recorded by each probe into m_t blocks p_m of time length T. Using a rectangular window, one has

$$R_{pp}(\boldsymbol{r},\omega) = \frac{2\pi}{T}\frac{1}{m_t}\sum_{m=1}^{m_t} \hat{p}_m(\boldsymbol{x}_0,\omega)\hat{p}_m^{\star}(\boldsymbol{x}_0+\boldsymbol{r},\omega)$$

The wavevector - frequency spectrum is then directly computed by discretizing the following Fourier integral,

$$\Phi_{pp}(\boldsymbol{k},\omega) = \frac{1}{(2\pi)^2}\iint R_{pp}(\boldsymbol{r},\omega) e^{-i\boldsymbol{k}\cdot\boldsymbol{r}} d\boldsymbol{r}$$

The transducer locations are denoted by $\boldsymbol{r}_{nm} = (d_n,\theta_m)$ in polar coordinates. For a given angle of the linear antenna, all the cross-spectra between the different microphones are available since the pressure signals are simultaneously recorded over the $n_p = 63$ probes. The irregular radial distribution of the microphones is presented in the next section. A regular polar distribution $\theta_m = m\Delta\theta$ has been chosen with $\Delta\theta = \pi/m_\theta$ and $m_\theta = 63$. In a straightforward approach, the wavenumber-frequency spectrum can be computed as

$$\Phi_{pp}(\boldsymbol{k},\omega) = \frac{1}{(2\pi)^2}\sum_{m=0}^{m_\theta-1}\sum_{n=0}^{n_r} R_{pp}(\boldsymbol{r}_{nm},\omega) e^{-i(k_1 d_n\cos\theta_m + k_2 d_n \sin\theta_m)} ds_n \tag{2}$$

over a given grid $\boldsymbol{k} = (k_1,k_2)$. In this particular and simple case, the central microphone corresponds to $d_0 = 0$, the location of a half of the linear antenna is defined by the radial distance d_n with $1 \le n \le 31$ and $n_r = (n_p+1)/2$. The corresponding elementary area can be written as

$$ds_n = \pi(l_{n+1}^2 - l_n^2) \times \frac{\Delta\theta}{2\pi} \qquad l_n = \frac{d_n + d_{n+1}}{2}$$

Pressure signals are recorded over the n_p probes at a sampling frequency of 51.2 kHz during a time length $T_0 = 90$ s. The cross-spectra are calculated with $m_t = 360$ blocks of time length $T = 250$ ms. There is therefore no overlap between the blocks. No windowing function has been applied to the data blocks. It has been found more efficient to apply a moving average to the cross-spectra $R_{pp}(\boldsymbol{r},\omega)$, with a variable filter width $\Delta f \sim f$.

B. Microphone array

As already mentioned, the principle of a linear array placed on a rotating disk has again been retained for this study. With respect to the study in Arguillat *et al.* [2], the size of the disk has been slightly increased to obtain a better resolution of low frequency components. Moreover a non-uniform radial distribution of the probes has also been chosen. An accurate description of the aerodynamic ridge requires a very small distance between probes, of the order of one millimeter, which can unfortunately not be obtained by using flush-mounted 1/4 or 1/8 inch microphones. Remote microphones have thus been selected in the present study, even if this solution also presents some drawbacks. A description of the microphone setting is provide in Appendix A.

A simple analytical model of the cross spectral density is considered for the characterization of the antenna response. The wavenumber-frequency spectrum calculated from expression (2) can then be compared to the exact solution. The cross spectral density $R_{pp}(\boldsymbol{\xi}, \omega)$ is defined as the sum of a diffuse sound field [13] and a convective component described by a Corcos model [14, 15] respectively, which yields

$$\begin{aligned} R_{pp}(\boldsymbol{\xi}, \omega) &= R_{pp}^{(a)}(\boldsymbol{\xi}, \omega) + R_{pp}^{(c)}(\boldsymbol{\xi}, \omega) \\ &= S(\omega)\frac{\sin(k_0\xi)}{k_0\xi} + A(\omega)e^{-(k_c/\alpha)|\xi_1|}e^{-(k_c/\beta)|\xi_2|}e^{ik_c\xi_1} \end{aligned} \tag{3}$$

where $\boldsymbol{\xi} = (\xi_1, \xi_2)$ is the separating vector. Classical values have been chosen for the two constants, namely $\alpha = 8$, and $\beta = 1$. The numerical test is performed for a free stream velocity $U_\infty = 50$ m.s^{-1}, a given frequency $f = 2000$ Hz, a convective wavenumber $k_c = 2\pi f/U_c$ with $U_c \simeq 0.7U_\infty$, an acoustic wave number $k_0 = 2\pi f/c_\infty$, and a relative amplitude between the two contributions of $S = 1$ and $A = 10^{-3}$. The corresponding spectrum $\Phi_{pp} = \Phi_{pp}^{(c)} + \Phi_{pp}^{(a)}$, refer to Appendix B for the details, is respectively given by

$$\Phi_{pp}^{(c)}(\boldsymbol{k}, \omega) = \frac{A(\omega)}{\pi^2}\frac{\alpha k_c}{k_c^2 + \alpha^2(k_1 - k_c)^2}\frac{\beta k_c}{k_c^2 + \beta^2 k_2^2} \tag{4}$$

and

$$\Phi_{pp}^{(a)}(\boldsymbol{k}, \omega) = \begin{cases} \dfrac{S(\omega)}{2\pi k_0^2}\dfrac{1}{\sqrt{1 - (k/k_0)^2}} & \text{if } k < k_0 \\ 0 & \text{if } k > k_0 \end{cases} \tag{5}$$

In Fig. 7, this analytical solution is compared to the response (2) provided by the antenna for the probe distribution used in a previous study [2], and also for the antenna retained in the present work. The linear antenna consists of $n_p = 63$ identical remote microphone probes, in order to reach a spacing of 1 mm near the antenna center. These probes are non-uniformly distributed along the disk diameter to optimize the antenna response to the wall pressure field (3). Note that the probe size $d_p = 0.5$ mm is reasonably small to reduce the spatial filtering as far as possible. Using the basic approach explained in section III A, a better resolution is obtained around the acoustic disk with this new distribution by removing oscillations in the

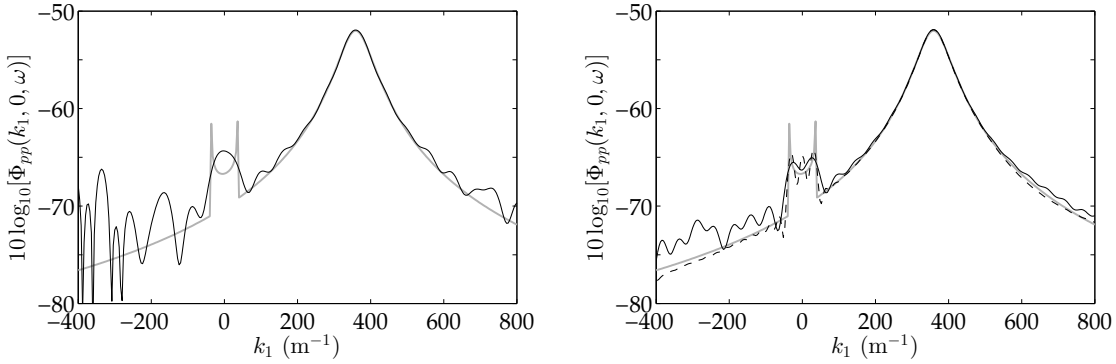

Fig. 7 Comparison between the anaytical expression —— given by expressions (5) - (4), and the antenna response —— given by integration of the Fourier integral (2). On the left, for the array used in Arguillat *et al.* [2]. On the right, for the array used in this study, and − − − response obtained by using all the possible separating vectors over the linear antenna.

subconvective region, as shown by the solid curve in Fig. 7. An accurate response can be achieved by using all the possible separating vectors over the antenna, as shown by the dashed curve in the same graph.

IV. Experimental results

A. Wall pressure spectra

In this section, the frequency power spectra of wall-pressure fluctuations $S_{pp}(\omega)$ are now considered. As detailed in the Appendix A, these spectra have been obtained using an 1/8 inch microphone, fit with a pinhole cap. The diameter of the cap hole is about $d_p \simeq 5$ mm. Following Corcos [14], all pressure spectra obtained using the pinhole microphone have been corrected to account for the spatial filtering of the sensor. The resulting pressure spectra are shown in Fig. 8 as black curves for a zero pressure gradient boundary layer. On the left, the measured spectra have been normalized by mixed variables. This leads to a collapse of the spectra in the low frequency domain. The spectra reach a maximum of about 5 dB for $\omega\delta_1/U_\infty$ around 0.4. Then, an $\omega^{-0.4}$ decay is observed in the range $0.5 < \omega\delta_1/U_\infty < 5$. Reynolds numbers are not high enough to observe the $\omega^{-0.7}$ power law. On the right, the measured spectra have been normalized by inner variables. This leads to a collapse of the spectra in the high-frequency domain $\omega\nu/{u_\tau}^2 > 0.6$, where an amplitude decay according to ω^{-5} can be distinguished.

The shape of the zero pressure gradient spectrum may be estimated by the semi-empirical model of Goody [27] given by

$$S_{pp}(\omega) \times \frac{U_\infty}{\tau_w^2 \delta} = \frac{C_2 {\omega_\delta}^2}{({\omega_\delta}^{0.75} + C_1)^{3.7} + (C_3\omega_\delta)^7} \qquad \omega_\delta = \frac{\omega\delta}{U_\infty} \geq 0 \tag{6}$$

with $C_1 = 0.5$, $C_2 = 5.0$, $C_3 = 1.1R_T^{-0.57}$ and where $R_T = (\delta/U_\infty)/(\nu/u_\tau^2)$ represents the

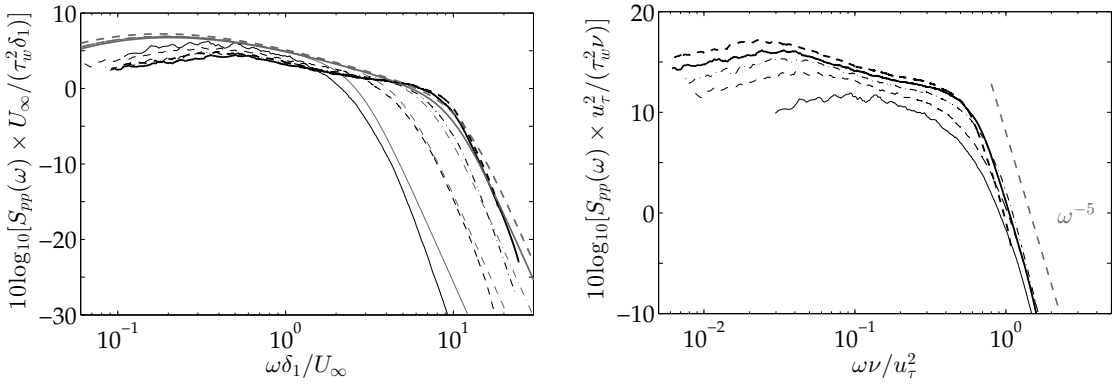

Fig. 8 Measured wall pressure spectra for a zero-pressure-gradient boundary layer. —— zpg11 case, – – – zpg25 case, –·–·– zpg36 case, —— zpg45 case, – – – zpg59 case, refer to Table 3 for boundary layer parameters. On the left, measured spectra normalized by mixed variables and comparison with Goody's model (6) in grey. On the right, measured spectra normalized by inner variables and comparison with the ω^{-5} power law.

ratio between outer and inner time scales, as Re^+ represents a similar ratio for length scales. The resulting model spectra have been plotted in Fig. 8 as grey curves. The Goody model is found to fit the experimental spectra within about 3 dB. The ability to predict the shape of the pressure spectrum in a wide range of Reynolds numbers is remarkable, since it can be easily synthesized to provide the excitation source for vibration problems [5] for instance.

The frequency power spectra of wall-pressure fluctuations are shown in Fig. 9 for the apg configuration (at left) and the fpg configuration (at right), normalized by outer variables. As was mentioned by other authors [16, 46], the shape of the pressure spectrum depends upon the mean pressure gradient. For the apg and fpg cases, the maximum values are about 8 dB and 3 dB, respectively, whereas it was of 5 dB for the ZPG case. The decay in the middle-frequency range is also modified.

The root-mean square pressure fluctuation, calculated as

$$p_{w,rms}^2 = \int_0^\infty S_{pp}(\omega) d\omega$$

and normalized by viscous scaling is plotted in Fig. 10 as a function of the Reynolds number $p_w^+ = f(\mathrm{Re}^+)$, and compared to previously published data. The normalized pressure fluctuations increase with the Reynolds number, as is the case for the previously published data [3, 15, 20, 26, 29, 36, 44]. The evolution of p_w^+ with Re^+ has also been described by Farabee and Casarella [21] using the following empirical law

$$p_w^{+2} = \begin{cases} 6.5 & (\mathrm{Re}^+ \leq 333) \\ 6.5 + 1.86\log(\mathrm{Re}^+/333) & (\mathrm{Re}^+ > 333) \end{cases} \quad (7)$$

In the present experiment, increasing the mean pressure gradient leads to an increase in p_w^+.

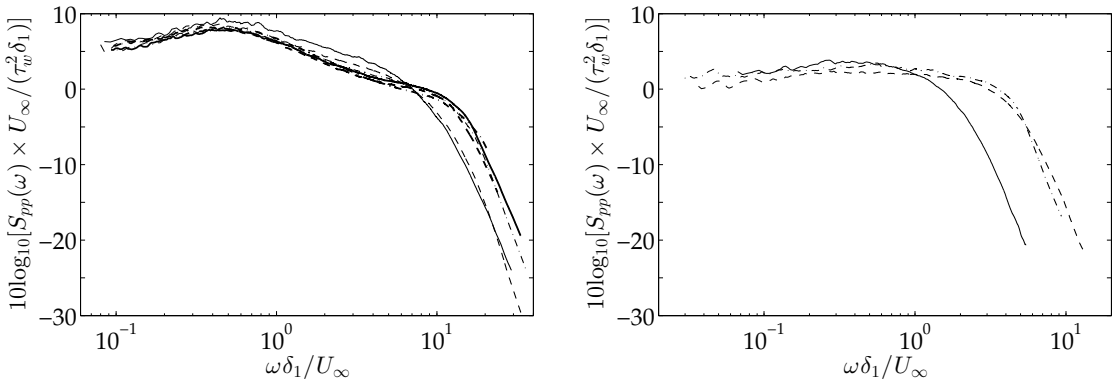

Fig. 9 On the left, measured spectra normalized by outer variables for the apg configuration. —— apg12 case, – – – apg19 case, –·–·– apg27 case, —— apg38 case, – – – apg45 case, –·–·– apg57 case. On the right, measured spectra normalized by outer variables for the fpg configuration. —— fpg10 case, – – – fpg32 case, –·–·– fpg45 case. Refer to Table 3 for boundary layer parameters.

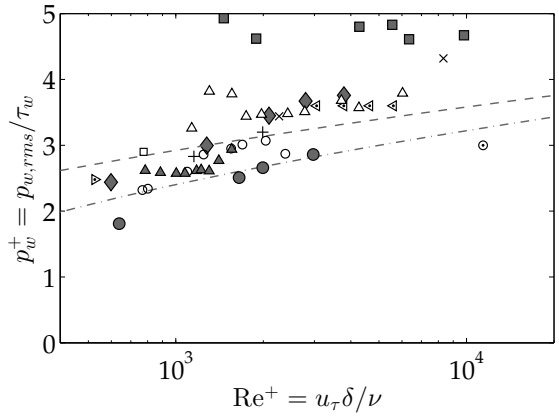

Fig. 10 Normalized root mean square wall pressure fluctuations p_w^+ as a function of the Reynolds number Re^+. ZPG-BL: ♦ present data, ⊙ Corcos [15], □ Emmerling *et al* [20], ◁ Blake [3], ▷Schewe [44], △ McGrath & Simpson [36], ○ Gravante *et al.* [29], + and – – – Eq. (7) from Farabee & Casarella [21], × Goody & Simpson [26], –·–·– Viazzo *et al.* (2001). APG-BL: ■ present data. FPG-BL: ● present data, ▲ McGrath & Simpson [36] for $-0.48 \leq \beta \leq -0.16$.

For the apg configuration, p_w^+ is of the order of 5, whereas it is of the order of 3 for the zpg configuration, and of 2 for the fpg configuration.

B. Convection velocity and length scales

In this section, the convection velocity U_c and the integral length scales L_1 and L_2 are extracted from the measured cross-spectra using the linear array of remote microphones. These quantities are defined from the term $R_{pp}^{(c)}(\xi, \omega)$ in Eq. (3). The convection velocity U_c is deduced

from a linear interpolation of the phase $\omega\xi_1/U_c$ in the cross-spectrum as illustrated by Fig. 11 (left). Due to the loss of coherence for the large separation distances ξ_1, the phase of the cross-spectrum is not linear over the whole ξ_1 range. The convection velocity was therefore estimated over a range of ξ_1 separations for which the phase is linear to within about 5%.

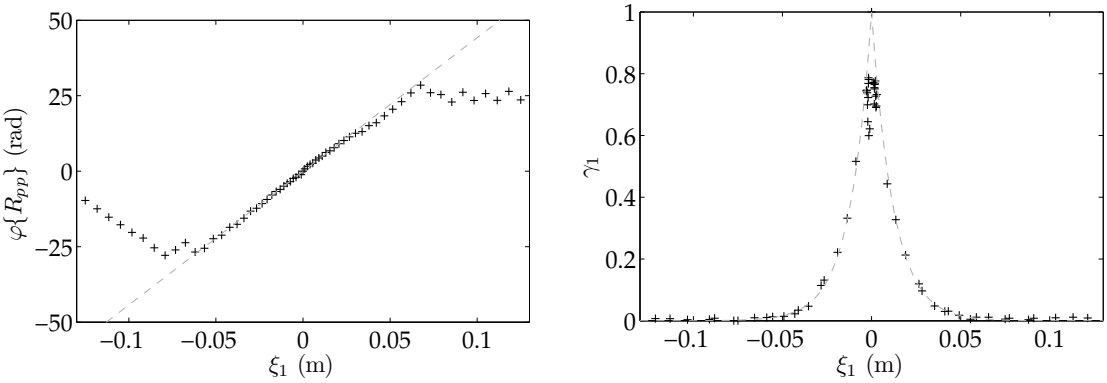

Fig. 11 Estimation of the Corcos parameters for the zpg45 case at a frequency $f = 2$ kHz. On the left, + cross-spectrum phase angle as a function of streamwise separation ξ_1, and – – –, linear fit for $-0.06 < \xi_1 < 0.06$. On the right, + streamwise coherence γ_1 as a function of ξ_1, and – – – exponential fit for -0.06 $< \xi_1 <$ 0.06.

The convection velocity is plotted in Fig. 12 (left) for the zpg25 and zpg45 cases, and compared to previously published data. The convection velocity increases with the frequency, then a maximum is reached, and the convection velocity decreases with the frequency, which is consistent with the literature. For the zpg configuration, the maximum value is $0.8U_\infty$ at $\omega\delta_1/U_\infty = 0.25$. The high-frequency limit is of about $0.6U_\infty$. For the apg and fpg configurations shown in Fig. 12 (right), the maximum convection velocity is increased. It is of about $0.85U_\infty$ at $\omega\delta_1/U_\infty = 0.25$ for the fpg configuration, and $0.9U_\infty$ at $\omega\delta_1/U_\infty = 0.60$ for the apg configuration.

According to Smol'yakov [47], the convection velocity can be predicted from the following empirical law

$$\frac{U_c}{U_\infty} = a\ \frac{\omega_{\delta_1}}{1 + b\omega_{\delta_1}^2} + c \tag{8}$$

with $\omega_{\delta_1} = \omega\delta_1/U_\infty$, $a = 1.6$, $b = 16$ and $c = 0.6$. The corresponding curve has been plotted in Fig. 12 (right). This empirical model is suitable for the zpg measurements, but not for the apg and fpg convection velocities. However, an excellent agreement is found between a *modified* Smol'yakov model and both the apg and fpg configurations by choosing $a = 0.8$, $b = 3$ and $c = 0.65$ for the apg configuration, and $a = 1.4$, $b = 20$ and $c = 0.7$ for the fpg configuration, see Fig. 12 (right). The theoretical dependence of these parameters is unknown, but they are expected to depend on the pressure gradient parameter β. A more complete study, together with numerical simulations, would lead to a better knowledge of this dependence in the future.

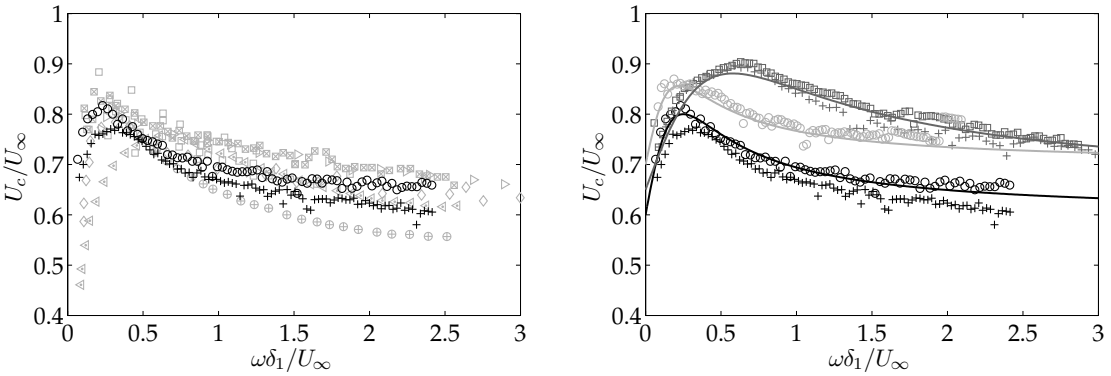

Fig. 12 Normalized convection velocity U_c/U_∞ as a function of dimensionless frequency $\omega\delta_1/U_\infty$. On the left, comparison between present zpg measurements and previously published data. ○ zpg25, + zpg45, ◁ Blake [3], ▷ Arguillat *et al* [2], ⊠ Abraham & Keith [1], □ Ibars [31], ⊕ Bull [7], ♢ Farabee & Casarella [21]. On the right, + apg38, □ apg57, ○ zpg25, + zpg45, ○ fpg32. —— Smolyakov model, —— modified Smolyakov model with $a = 0.8$, $b = 3$ and $c = 0.65$, —— modified Smolyakov model with $a = 1.4$, $b = 20$ and $c = 0.7$.

The characteristic length scales of the flow are also deduced from cross-spectra measurements. First, the cross-spectra are normalized as a coherence function denoted γ and defined as

$$\gamma^2(\boldsymbol{\xi},\omega) = \frac{|R_{pp}(\boldsymbol{\xi},\omega)|^2}{S_{pp}(\boldsymbol{x},\omega)S_{pp}(\boldsymbol{x}+\boldsymbol{\xi},\omega)} \tag{9}$$

The coherence is a function of the frequency ω and of the separating vector $\boldsymbol{\xi}$ between the two power spectra $S_{pp}(\boldsymbol{x},\omega)$ and $S_{pp}(\boldsymbol{x}+\boldsymbol{\xi},\omega)$. Assuming that the pressure field is homogeneous, the streamwise coherence function γ_1 is deduced from the expression of $R_{pp}^{(c)}(\boldsymbol{\xi},\omega)$ in Eq. (3) as

$$\gamma_1 = \gamma(\xi_1, \xi_2 = 0, \omega) = \exp\left(\frac{-|\xi_1|}{L_1}\right) \tag{10}$$

The transverse coherence function γ_2 is defined as a function of ξ_2 and L_2 in the same way. The longitudinal and transverse length scales, respectively L_1 and L_2, are then estimated from coherence measurements by fitting the measured coherence functions, respectively γ_1 and γ_2, by an exponential profile. As an example, the measured coherence function γ_1 is shown in Fig. 11 (right) as a function of ξ_1 for the zpg45 case, at a frequency $f = 2$ kHz. An excellent agreement is found with an exponential profile in the range -0.06 $< \xi_1 <$ 0.06, and the length scale L_1 can be determined from Eq. (10).

Both longitudinal and transverse length scales are displayed in Fig. 13 as a function of dimensionless frequency. In the present experiment, both length scales reach a maximum of about $20\delta_1$ in the streamwise direction and $4\delta_1$ in the transverse direction. They also decrease with the frequency at an ω^{-1} rate, as predicted by Corcos [15]. According to Corcos, the length

scales are expected to vary as

$$L_1 = \frac{\alpha U_c}{\omega} \quad \text{and} \quad L_2 = \frac{\beta U_c}{\omega}$$

with the standard values $\alpha = 8$ and $\beta = 1$, which can be re-written to match the normalization used in the present study as

$$\frac{L_1}{\delta_1} = \frac{\alpha}{\tilde{\omega}} \frac{U_c}{U_\infty} \quad \text{and} \quad \frac{L_2}{\delta_1} = \frac{\beta}{\tilde{\omega}} \frac{U_c}{U_\infty}$$

It has already been noticed that this expression is only valid for high frequencies. Indeed, at very low frequencies, the resulting length scales would be larger than the boundary layer thickness. As shown in Fig. 13, an excellent agreement is found with the experimental values under the assumption that $\omega\delta_1/U_\infty > 0.4$.

A empirical model has been proposed by Efimtsov [18] to correct the low-frequency scales. The two integral length scales are provided by

$$\frac{L_1}{\delta} = \left[\left(\frac{a_1 \omega_e}{U_c/u_\tau} \right)^2 + \frac{{a_2}^2}{{\omega_e}^2 + (a_2/a_3)^2} \right]^{-1/2} \qquad \frac{L_2}{\delta} = \left[\left(\frac{a_4 \omega_e}{U_c/u_\tau} \right)^2 + \frac{{a_5}^2}{{\omega_e}^2 + (a_5/a_6)^2} \right]^{-1/2}$$

respectively, with $\omega_e = \omega\delta/u_\tau$, $a_1 = 0.1$, $a_2 = 72.8$, $a_3 = 1.54$, $a_4 = 0.77$, $a_5 = 548$ and $a_6 = 13.5$. These expressions can be recast to introduce δ_1 rather than δ as length scale for instance. This yields

$$\frac{L_1}{\delta_1} = \left[\left(\frac{a_1 \omega_{\delta_1}}{U_c/U_\infty} \right)^2 + \frac{{a_2}^2}{\omega_{\delta_1}^2 \left(H_1^2 U_\infty^+ \right)^2 + (a_2/a_3)^2} \right]^{-1/2}$$

$$\frac{L_2}{\delta_1} = \left[\left(\frac{a_4 \omega_{\delta_1}}{U_c/U_\infty} \right)^2 + \frac{{a_5}^2}{\omega_{\delta_1}^2 \left(H_1^2 U_\infty^+ \right)^2 + (a_5/a_6)^2} \right]^{-1/2}$$

with $H_1 = \delta/\delta_1$. It has been reported [39] that the nominal values a_1 to a_6 provided by Efimtsov have to be modified to obtain the right length scales. It is also the case in the present study. As illustrated in Fig. 13, a good agreement is found between the measurements and this model with $a_1 = 0.18$, $a_2 = 15$ and $a_3 = 0.13$, $a_4 = 0.85$, $a_5 = 100$ and $a_6 = 1$. These values have been obtained in the present study under two assumptions. First, as $\omega_{\delta_1} \to \infty$, the Efimtsov model should reach the values predicted by Corcos. Second, if $\omega_{\delta_1} \to 0$, $L_1/\delta_1 \to 9$ in order to ensure that the longitudinal length scale remains smaller than the boundary layer thickness. The resulting curves of this *modified* Efimtsov empirical law are plotted in Fig. 13. Note that the constants a_1 to a_6 are kept the same between the three configurations (apg, zpg and fpg). The differences between these three configurations are induced by the differences in convection velocities, see Fig. 12 (right). An excellent agreement is found between the *modified* Efimtsov model and the transverse length scale L_2. For the longitudinal length scale, the agreement is worse, especially in the middle frequency domain $0.2 < \omega_{\delta_1} < 0.6$, where the longitudinal length scale seems to depend on the mean pressure gradient.

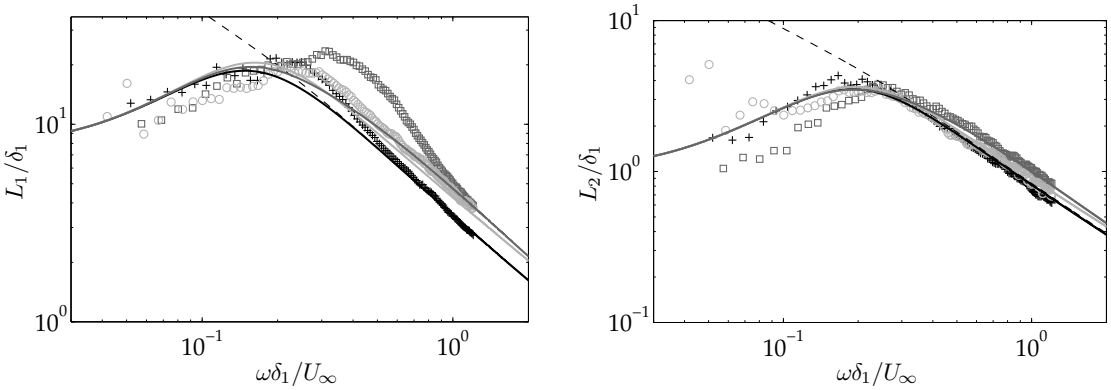

Fig. 13 Normalised longitudinal L_1/δ_1 and transverse L_2/δ_1 scales as a function of ω_{δ_1}. Present measurements: □ apg57, + zpg45, ○ fpg32; − − − Corcos model with α =5 and β =1.2; ——, —— and —— modified Efimtsov model with $a_1 = 0.18$, $a_2 = 15$, $a_3 = 0.13$, $a_4 = 0.85$, $a_5 = 100$ and $a_6 = 1$, for the apg57, zpg45 and fpg32 cases respectively.

C. Wavenumber-frequency spectra

The wavenumber-frequency spectra $\Phi_{pp}(\boldsymbol{k},\omega)$ have been extracted from the line array measurements using Equation (2). Three examples are shown in Fig. 14 for the apg19, zpg45 and fpg32 cases. Note that these three examples are measured at the same dimensionless frequency $\omega\delta_1/U_\infty = 0.42$. This value has been chosen to maximize wall-pressure fluctuations in the three configurations, see Fig. 8 (left) and Fig. 9. The wavenumber spectra exhibit a convective ridge centered around the convective wavenumber $k_c = 2\pi f/U_c$. For the three mentioned configurations, an acoustic component can also be distinguished at low wavenumbers.

The streamwise one-dimensional wavenumber-frequency $\Phi^{(1)}_{pp}(k_1,\omega)$, defined as

$$\Phi^{(1)}_{pp}(k_1,\omega) = \int_{-\infty}^{+\infty} \Phi_{pp}(\boldsymbol{k},\omega)dk_2$$

is shown as a function of frequency in Fig. 15. The convective ridge, located around the convective wavenumber $k_c = 2\pi f/U_c$, is shifted towards higher k_1 as the frequency is increased. The position $k_c\delta_1$ of the convective ridge has been detected from the one-dimensional wavenumber spectra. The convection velocity has therefore been estimated as

$$\frac{U_c}{U_\infty} = \frac{1}{k_c\delta_1}\omega_{\delta_1}$$

The results, plotted in Fig. 15 at right for the zpg25, zpg45, zpg76 and zpg100 cases, are consistent with the estimation of the convection velocity made in section IV.B, see in particular Fig. 12. The acoustic component, already identified in Fig. 14, is visible in the range $0 < \omega_{\delta_1} < 1$. The amplitude of the acoustic component rapidly decreases with the frequency. The estimation of the acoutic contribution to wall-pressure fluctuations is currently in progress.

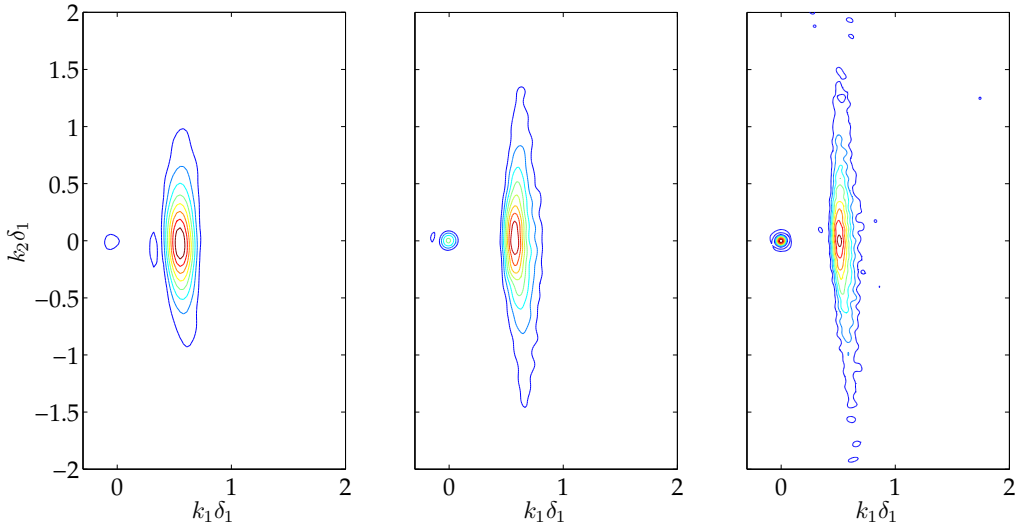

Fig. 14 Normalised wavevector-frequency spectra $\Phi_{pp}(k,\omega) \times U_\infty/({\tau_w}^2{\delta_1}^3)$, measured for the same frequency $\omega\delta_1/U_\infty = 0.42$. On the left, apg19 case, isocontours between 0 and 16 with a step of 2. Center, zpg45 case, isocontours between 0 and 4 with a step of 0.5. On the right, fpg32 case, isocontours between 0 and 4 with a step of 0.5.

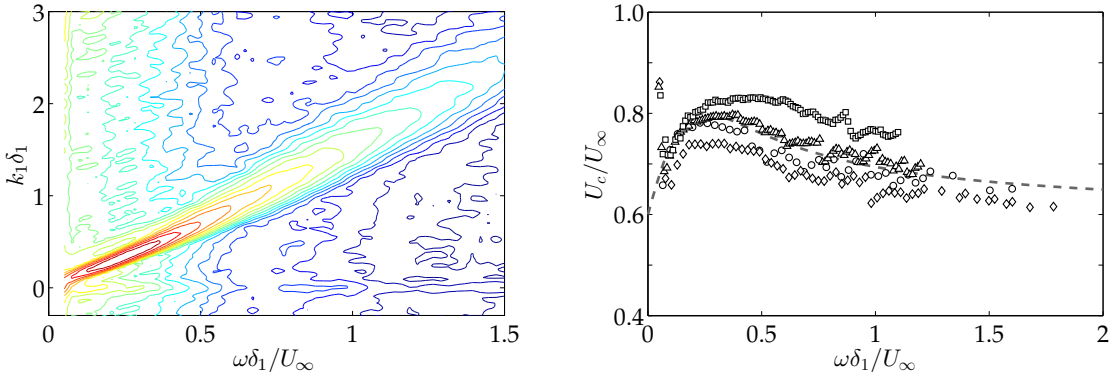

Fig. 15 On the left, normalised zpg45 one-dimensionnal wavevector-frequency spectra $\Phi^{(1)}_{pp}(k_1,\omega) \times U_\infty/({\tau_w}^2{\delta_1}^2)$ in decibels, as a function of frequency $\omega\delta_1/U_\infty$. Isocontours between -9 dB and 9 dB, with a step of 1 dB. On the right, frequency dependence of the convection velocity determined from streamwise spectra $\Phi^{(1)}_{pp}(k_1,\omega)$ for the zpg configuration, ○ zpg25, ◊ zpg45, △ zpg76, □ zpg100 and - - - comparison with Smol'yakov empirical law (8).

V. Concluding remarks

Wall pressure fluctuations beneath a turbulent boundary layer in the presence of a mean pressure gradient have been investigated in this study. A new channel was designed for flow-acoustic measurements. Some properties of the turbulent flow have been determined for zero-pression-gradient boundary layers as well as for adverse- and favorable-pressure-gradient con-

figurations. Wall pressure fluctuations have also been measured using a pinhole microphone combined to an original high-frequency calibration. They have been found in good agreement with previous experimental data. Direct measurements of wavevector-frequency spectra have been performed with the use of a rotating linear antenna of remote microphones. The microphone distribution has been optimized to improve the array response with respect to previous works. The convection velocity or length scales associated with the aerodynamic contribution have been extracted from the data and compared to other measurements and some classical models. Effects induced by the presence of a mean pressure gradient have been exhibited and it has been shown that a parametrization seems possible. Moreover, an acoustic contribution is identified from the reconstruction of the wavevector-frequency spectrum.

The present work is still in progress to rebuild wavenumber-frequency spectra using all the properties of the rotating antenna. Furthermore, the extraction of the acoustic part requires additional efforts and is also currently being examined. Finally, the modelling of pressure spectra and of the convective ridge in the presence of a mean pressure gradient appears tricky in the sense that the isolated role of each turbulent flow parameter needs to be reasonably identified. Numerical simulations should be cleverly combined with experimental studies to provide such models in the future.

Acknowledgments

This research has been funded by the Agence Nationale de la Recherche through the ANR-2011-BS09-035-02 project SONOBL, and also by the Labex CeLyA of Université de Lyon, operated by the French National Research Agency (ANR-10-LABX-0060/ ANR-11-IDEX-0007). The authors wish to express their most sincere thanks to Jean-Michel Perrin, Pierre Roland and Pascal Souchotte for their help in setting up the experiment.

APPENDIX A: MICROPHONE PROBES

Calibration of the pinhole microphone

An 1/8 inch Brüel & Kjær type 4138 microphone has been used for measuring wall pressure spectra in order to obtain a high-frequency response. The sensing area of the microphone has been reduced by fitting it with a pinhole mask made of a perforated cap, as shown in Figure 16. The diameter of the pinhole is about $d_p \simeq 0.5$ mm. The frequency cutoff of such a mounting is fixed by the frequency cutoff of the cavity inside the cap. This cavity behaves more or less like a Helmholtz resonator [23], but it is rather illusory to theoretically predict the resonance frequency f_r of such a geometry. The resonance frequency is observed to be $f_r \simeq 21$ kHz.

The low frequency response of the pinhole microphone is obtained by following a two-step procedure. A loudspeaker is used to generate a white noise in the frequency range from 10 Hz to 15 kHz, which propagates through a calibration tube, as sketched in Figure 17. A reference microphone is also mounted near the open end of the calibration tube. In the first step, the calibration tube sketched in Figure 17 is positioned above the pinhole microphone to be

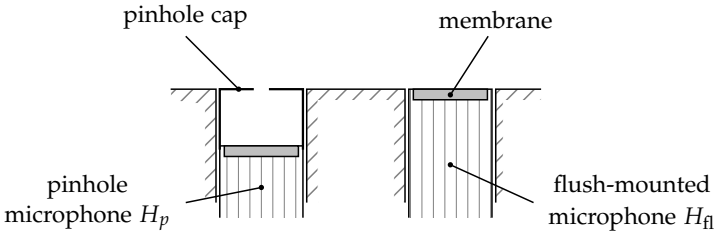

Fig. 16 Sketch of the pinhole microphone and of the flush-mounted microphone used for the calibration.

calibrated. The complex transfer function $F_1 = H_p/H_{\mathrm{ref}}$ between the pinhole microphone and the reference microphone is measured. In the second step, the calibration tube is positioned above an 1/8 inch Brüel & Kjær microphone type 4138 flush-mounted into a plane baffle, see Figure 16. The transfer function $F_2 = H_{\mathrm{fl}}/H_{\mathrm{ref}}$ between the flush-mounted microphone and the reference microphone is then measured. Assuming that the frequency response of the flush-mounted microphone is flat, that is $H_{\mathrm{fl}} \simeq 1$, the frequency response of the remote probe is obtained by dividing the two measured transfer functions, $H_p = F_1/F_2$. This method is valid up to the cutoff frequency of the calibration tube, which is of about 17 kHz and the transfer function H_p is plotted in solid gray line in Figure 18.

As mentioned above, the cutoff frequency of the pinhole microphone imposed by the Helmholtz resonator is higher. A second calibration method has thus been used to recover the high frequency part of the transfer function H_p, ranging from 15 kHz to 30 kHz. A short duration and high pressure shock wave is generated by an electric spark source.[41, 43] The spark source is made of two tungsten electrodes, separated by a gap of 20 mm, connected to a high voltage supply. The pinhole microphone and the flush-mounted microphone are placed at the same distance of the spark source, see again Figures 16 and 17. Assuming that the frequency response of the flush-mounted microphone is flat, the high-frequency response of the pinhole microphone is then measured up to 50 kHz, as shown in dashed gray line in Figure 18. Finally, the two calibration curves are combined to derive the whole transfer function H_p of the pinhole microphone.

The calibration is performed without flow, but the hump associated with the pinhole cap depends appreciably on the mean velocity of the flow. To overcome this difficulty, the final transfer function has been parametrized[25] with a second-order low-pass filter

$$H(f) = \frac{S_0}{1 + \frac{i}{q}(f/f_r) - (f/f_r)^2}$$

where $q = q(U_\infty)$ is the quality factor, $f_r = f_r(U_\infty)$ the resonance frequency and S_0 a constant.

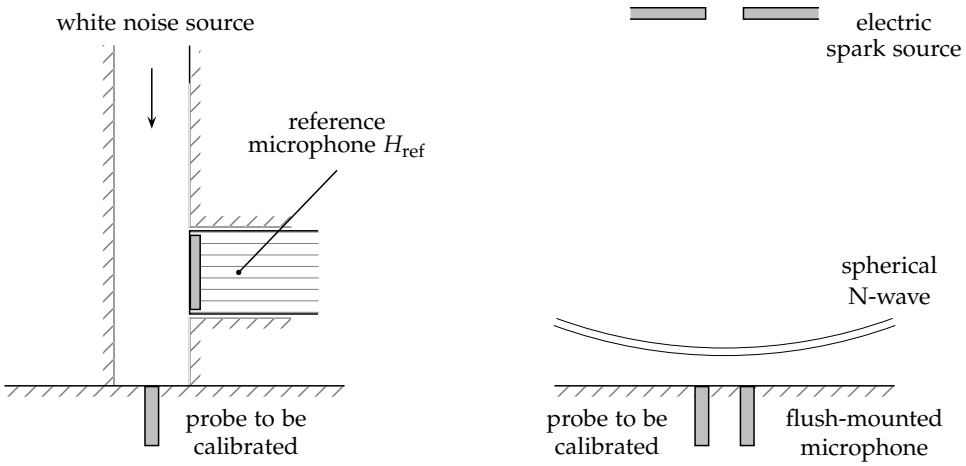

Fig. 17 On the left, sketch of the calibration tube used up to the cutoff frequency of the tube. On the right, high-frequency calibration using a spark source.

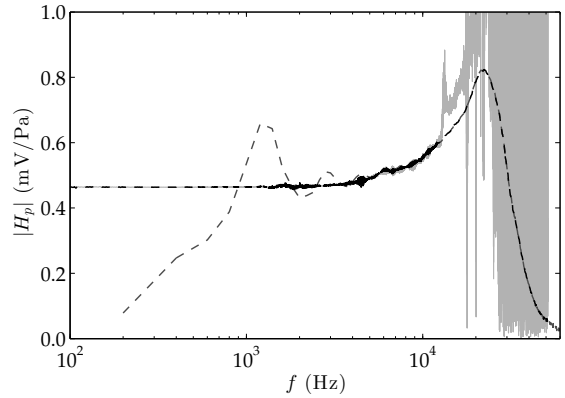

Fig. 18 Transfer function $H_p(f)$ of the pinhole microphone in black dashed line, obtained by combining the response of the probe to a white noise source in the range 10 Hz - 15 kHz in solid gray line, and the response to the spark source in the range 3 kHz - 50 kHz in dashed gray line.

Remote microphone probes

The pressure antenna is composed of 63 identical remote microphone probes, and each remote probe contains an 1/4 inch Brüel & Kjær type 4957 microphone, whose cutoff frequency is of about 15 kHz. The microphone is placed on the edge of steel tubes of variable diameter, as illustrated in Figure 19. The diameter of the last steel tube, fit flush onto the surface of the rotating disk, is of 0.5 mm. A two-meter long rear tube made of vinyl is used to dissipate pressure fluctuations and therefore avoid acoustic reflections. An advantage of such a microphone mounting is to reduce the sensing area of the probe, and consequently to limit the spatial averaging caused by the sensor. It also permits to reduce the spacing between two neighbour

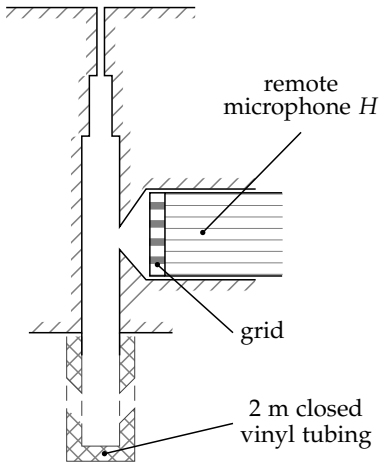

Fig. 19 Sketch of a remote microphone probe used to build the disk antenna.

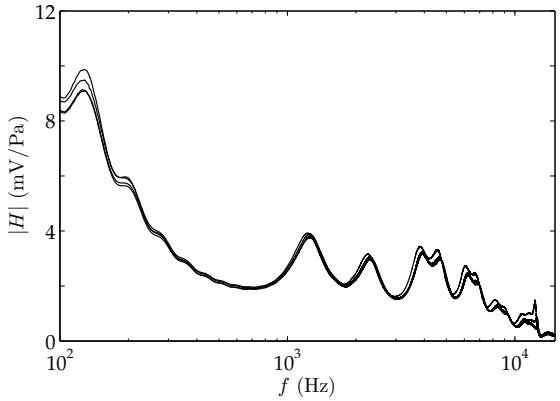

Fig. 20 Transfer function H of one remote microphone probe of the disk antenna, measured four times at different days during the present experiments.

probes.

The first calibration method presented in the previous section is applied to get the transfer function H of each remote probe. There is no need to perform a high-frequency calibration using a spark source since the cutoff frequency of the calibration tube is here higher than the microphone cut-off frequency. The transfer function of one given probe is shown in figure 20 to demonstrate that small variations are identified. Note that the amplitude is plotted using a linear scale.

Transducer resolution correction

All the pressure spectra have been corrected by using the data provided by Corcos [14] to take account of the spatial integration over the sensing area imposed by the pinhole [35]. The dimensionless pinhole diameter ranges in the interval $16 \leq d_p^+ \leq 68$ for the zero-pressure-gradient boundary layers investigated in the present study. According to Schewe [44] or Gravante *et al.* [29] among others, the spatial averaging attenuates high-frequencies up to $\omega^+ \simeq 1$ for $d_p^+ \geq 19$. The spectral correction is applied using the dimensionless frequency $S_p = \omega d_p/(2U_c)$ with $U_c = 0.6U_\infty$, and by stressing that $S_p \leq 2.1$ here.

APPENDIX B: WAVEVECTOR-FREQUENCY PRESSURE SPECTRUM OF A DIFFUSE SOUND FIELD

The wall pressure spectrum $\Phi_{pp}(\boldsymbol{k}, \omega)$ of a stationary and isotropic acoustic field is briefly derived in what follows. For an harmonic plane wave $p(\boldsymbol{x}, t) = Ae^{i(\boldsymbol{k}_0 \cdot \boldsymbol{x} - \omega_0 t)}$ of pulsation ω_0, of wavenumber $k_0 = \omega_0/c_\infty$ and of incidence angle θ, defined as the angle between the normal to the wave fronts and the plane $x_3 = 0$, the cross-correlation function between two points located at $\boldsymbol{x}$ and $\boldsymbol{x} + \boldsymbol{r}$ in this plane is given by

$$R_{pp}(\boldsymbol{r}, \tau) = E[(p(\boldsymbol{x}, t)p^\star(\boldsymbol{x} + \boldsymbol{r}, t + \tau)] = \frac{A^2}{2} e^{i(\boldsymbol{k}_0 \cdot \boldsymbol{r} - \omega_0 \tau)}$$

All the directions must be taken into account for an isotropic field. By averaging the factor $e^{i(\boldsymbol{k}_0 \cdot \boldsymbol{r})}$ over all the directions of an half-sphere [13], one gets

$$\frac{1}{2\pi} \int_0^\pi \int_0^\pi e^{i(\boldsymbol{k}_0 \cdot \boldsymbol{r})} \sin\theta d\varphi d\theta = \frac{1}{2} \int_\pi^0 e^{ik_0 r \cos\theta} d(\cos\theta) = \frac{\sin(k_0 r)}{k_0 r}$$

and the correlation function of a diffuse sound field is thus given by

$$R_{pp}(\boldsymbol{r}, \tau) = \frac{A^2}{2} \frac{\sin(k_0 r)}{k_0 r} \cos(\omega_0 \tau)$$

The cross-spectrum is then calculated by taking the Fourier transform, which yields

$$S_{pp}(\boldsymbol{r}, \omega) = \frac{A^2}{2} \frac{\sin(k_0 r)}{k_0 r} \frac{1}{2\pi} \int_{-\infty}^{+\infty} \cos(\omega_0 \tau) e^{i\omega\tau} d\tau = \frac{A^2}{4} \frac{\sin(k_0 r)}{k_0 r} \left[\delta(\omega - \omega_0) + \delta(\omega + \omega_0)\right]$$

The wavenumber-frequency spectrum is then obtained by taking the Fourier transform of $S_{pp}(\boldsymbol{r}, \omega)$. The space Fourier transform of the cardinal sine function is first considered. One has

$$\frac{1}{(2\pi)^2} \iint \frac{\sin(k_0 r)}{k_0 r} e^{-i\boldsymbol{k} \cdot \boldsymbol{r}} d\boldsymbol{r} = \frac{1}{(2\pi)^2} \iint \frac{\sin(k_0 r)}{k_0 r} e^{-ikr\cos\theta} r d\theta dr = \frac{1}{2\pi k_0} \int_0^\infty \sin(k_0 r) J_0(kr) dr$$

and the integral function is given by [50]

$$\int_0^\infty \sin(k_0 r) J_0(kr) dr = \begin{cases} \dfrac{1}{(k_0^2 - k^2)^{1/2}} & k < k_0 \\ 0 & k > k_0 \end{cases}$$

Finally, the wall pressure spectrum of an harmonic diffuse field of pulsation ω_0 can be written as

$$\Phi_{pp}(\boldsymbol{k},\omega_0) = \begin{cases} 2\dfrac{A^2}{4}\dfrac{1}{2\pi k_0^2}\dfrac{1}{\sqrt{1-(k/k_0)^2}} & k < k_0 \\ 0 & k > k_0 \end{cases}$$

where the factor 2 is introduced to obtain a single-sided frequency spectrum, the convention used in this paper. This expression corresponds to Eq. (5).

REFERENCES

[1] Abraham, B. M. & Keith W. L., 1998, Direct measurements of turbulent boundary layer wall pressure wavenumber-frequency spectra, *J. Fluid Eng.*, **120**, 29-39.

[2] Arguillat, B., Ricot, D., Bailly, C. & Robert, G., 2010, Measured wavenumber - frequency spectrum associated with acoustic and aerodynamic wall pressure fluctuations, *J. Acoust. Soc. Am.*, **128**(4), 1647-1655.

[3] Blake, W. K., 1970, Turbulent boundary-layer wall-pressure fluctuations on smooth and rough walls, *J. Fluid Mech.*, **44**(4), 637-660.

[4] Blake, W. K., 1986, Essentials of turbulent wall-pressure fluctuations, in Mechanics of flow-induced sound and vibration, Vol. II Complex flow-structure interactions, *Academic Press Inc.*, Orlando, Florida.

[5] Bremner, P. G. & Wilby, J. F., 2002, Aero-vibro-acoustics: problem statement and methods for simulation-based design solution, 8th AIAA/CEAS Aeroacoustics Conference, AIAA Paper 2002-2551.

[6] Bremner, P., 2014, Developing aerodynamic design diagnostics for control of interior wind noise, Proceedings of the 14ème Congrès Français d'Acoustique, 22-25 avril, Poitiers, France, 2139-2146.

[7] Bull, M. K., 1967, Wall pressure fluctuations associated with subsonic turbulent boundary layer flows, *J. Fluid Mech.*, **28**(4), 719-754.

[8] Bull, M. K., 1996, Wall-pressure fluctuations beneath turbulent boundary layers: some reflections on forty years of research, *J. Sound Vib.*, **190**(3), 299-315.

[9] Chauhan, K. A., Monkewitz, P. A. & Nagib, H. M., 2009, Criteria for assessing experiments in zero pressure gradient boundary layers, *Fluid Dyn. Res.*, **41**, 021404, 1-23.

[10] Cipolla, K. & Keith, W., 2000, Effects of pressure gradients on turbulent boundary layer wave number frequency spectra, *AIAA Journal*, **38**(10), 1832-1836.

[11] Clauser, F. H., 1954, Turbulent boundary layers in adverse pressure gradients, *Journal of the Aeronautical Sciences*, **21**, 91-108.

[12] Coles, D., 1956, The law of the wake in the turbulent boundary layer, *J. Fluid Mech.*, **1**, 191-226.

[13] Cook, R. K., Waterhouse, R. V., Berendt, R. D., Edelman, S. & Thompson Jr, M. C., 1955, Measurements of correlation coefficients in reverberant sound fields, *J. Acoust. Soc. Am.*, **27(6)**, 1072-1077.

[14] Corcos, G. M., 1963, Resolution of pressure in turbulence, *J. Acous. Soc. Am.*, **35**(2), 192-199.

[15] Corcos, G. M., 1964, The structure of the turbulent pressure field in boundary-layer flows, *J. Fluid Mech.*, **18**(3), 353-378.

[16] DeJong, R. G. & Kuiper, I. J., 2012, Pressure gradient effects on turbulent pressure spectrum Proceedings of InterNoise 2012, 19-22 august, New York City, USA.

[17] Dixit, S. A. & Ramesh, O. N., 2008, Pressure-gradient-dependent logarithmic laws in sink flow turbulent boundary layers, *J. Fluid Mech.*, **615**, 445-475.

[18] Efimtsov, B. M., 1982, Characteristics of the field of turbulent wall pressure fluctuations at large Reynolds numbers, *Sov. Phys. Acoust.*, **28**(4), 289-292.
[19] Ehrenfried, K. & Koop, L., 2008, Experimental study of pressure fluctuations beneath a compressible turbulent boundary layer, 14th AIAA/CEAS Aeroacoustics Conference, AIAA Paper 2008-2800.
[20] Emmerling, R., Meier, G. E. A. & Dinkelacker, A., 1973, Investigation of the instantaneous structure of the wall pressure under a trubulent boundary layer flow, *Agard*, Conference Proceedings No. 131, on Noise Mechanisms, 21-1 - 24-12.
[21] Farabee, T. M. & Casarella, M. J., 1991, Spectral features of wall pressure fluctuations beneath turbulent boundary layer, *Phys. Fluids A*, **3**(10), 2410-2420.
[22] Gabriel, C., Müller, S., Ullrich, F. & Lerch, R., 2014, A new kind of sensor arry for measuring spatial coherence of surface pressure on a car's side window, *J. Sound Vib.*, **333**, 901-915.
[23] Gallas, Q., 2005, On the modeling and design of zero-net mass flux actuators, PhD Thesis, University of Florida.
[24] Gloerfelt, X. & Berland, J., 2013, Turbulent boundary-layer noise: direct radiation at Mach number 0.5, *J. Fluid Mech.*, **723**, 318-351.
[25] Goody, M. C., 1999, An experimental investigation of pressure fluctuations in three-dimensional turbulent boundary layers, Ph.D. Dissertation, Virginia Polytechnic Inst. and State Univ. Blackburg, VA.
[26] Goody, M. C. & Simpson, R. L., 2000, Surface pressure fluctuations beneath two- and three-dimensional turbulent boundary layers, *AIAA Journal*, **38**(10), 1822-1831.
[27] Goody, M., 2004, Empirical spectral model of surface pressure fluctuations, *AIAA Journal*, **42**(9), 1788-1794.
[28] Graham, W. R., 1997, A comparison of models for the wavenumber-frequency spectrum of turbulent boundary layer pressures, *J. Sound Vib.*, **206**(4), 430-454.
[29] Gravante, S. P., Naguib, A. M., Wark, C. E. & Nagib, H. M., 1998, Characterization of the pressure fluctuations under a fully developed turbulent boundary layer, *AIAA Journal*, **36**(10), 1808-1816.
[30] Hu, Z., Morfey, C. L. & Sandham, N. D., 2006, Sound radiation from a turbulent boundary layer, *Phys. Fluids*, **18**, 098101, 1-4.
[31] Ibars P., 1990, Contribution des petits nombres d'onde au champ pariétal de pression dans une couche limite turbulente bidimensionnelle. Comparaison de différentes techniques expérimentales. *Ph.D. Thesis*, Ecole Centrale de Lyon, No. 90-15 (in french).
[32] Kremer, F., Bogey, C. & Bailly, C., 2014, Semi-implicit Runge-Kutta schemes: development and application to compressible channel flow, *AIAA Journal*, 52(3), 516-527.
[33] Keith, W. L., Hurdis, D. A. & Abraham, B. M., 1992, A comparison of turbulent boundary layer wall-pressure spectra, *Journal of Fluids Engineering*, **114**, 338-347.
[34] Leclercq, D. J. J. & Bohineust, X., 2002, Investigation and modelling of the wall pressure field beneath a turbulent boundary layer at low and medium frequencies, *J. Sound Vib.*, **257**(3), 477-501.
[35] Maidanick, G., 1967, Flush-Mounted pressure transducer systems as spatial and spectral filters, *J. Acoust. Soc. Am.*, **42**(5), 1017-1024.
[36] McGrath, B. E. & Simpson, R. L., 1987, Some features of surface pressure fluctuations in turbulent boundary layers with zero and favorable pressure gradients, NASA-CR-4051.
[37] Monty, J. P., Harun, Z. & Marusic, I., 2011, A parametric study of adverse pressure gradient turbulent boundary layers, *Int. Journal of Heat and Fluid Flow*, **32**, 575-585.
[38] Nagano, Y. & Houra, T., 2002, Higher-order moments and spectra of velocity fluctuations in adverse-pressure-gradient turbulent boundary layer, *Exp. Fluids*, **33**, 22-30.
[39] Palumbo, D., 2012, Determining correlation and coherence lengths in turbulent boundary layer flight

data, *J. Sound Vib.*, **331**, 3721-3737.

[40] Panton, R. L. & Robert, G., 1994, The wavenumber-phase velocity representation for the turbulent wall-pressure spectrum, *Journal of Fluid Engineering*, **480**(116), 477-483.

[41] Ollivier, S., Salze, E., Averiyanov, M., Yuldashev, P., Khokhlova, V., & Blanc-Benon, P., 2012, Calibration method for high frequency microphones, *Acoustics 2012*, 13-17 April, Nantes, 3503-3507.

[42] Rozenberg, Y., Robert, G. & Moreau, S., 2012, Wall-pressure spectral model including the adverse pressure gradient effects, *AIAA Journal*, **50**(10), 2168-2179.

[43] Salze, E., Ollivier, S., Blanc-Benon, P., Yuldashev, P., Averiyanov, M., & Khokhlova, V., 2011, Characterisation of the sound field emitted by an electric spark source in air, *6th Forum Acusticum*, ACUSTICUM2011/285 Aalborg, Denmark, June 27-July 1st.

[44] Schewe, G., 1983, On the structure and resolution of wall-pressure fluctuations associated with turbulent boundary-layer flow, *J. Fluid Mech.*, **134**, 311-328.

[45] Schlichting, H. & Gersten, K., 2000, *Boundary layer theory*, Springer-Verlag, Berlin Heidelberg.

[46] Schloemer, H. H., 1967, Effects of pressure gradient on turbulent-boundary-layer wall-pressure fluctuations, *J. Acoust. Soc. Am.*, **42**(1), 93-113.

[47] Smol'yakov, A. V., 2006, A new model for the cross spectrum and wavenumber-frequency spectrum of turbulent pressure fluctuations in a boundary layer, *Acoustical Physics*, **52**(3), 331-337.

[48] Sevik, M. M., 1986, Topics in hydro-acoustics, in *Aero- and Hydro-Acoustics*, Springer-Verlag Berlin, 285-308.

[49] Viazzo, S., Dejoan, A. & Schiestel, R., 2001, Spectral features of the wall-pressure fluctuations in turbulent wall flows with and without perturbations using LES, *Int. J. Heat Fluid Flow*, **22**, 39-52.

[50] Watson, G. N., 1966, *A treatise of the theory of Bessel functions*, Cambridge University Press, London.

[51] Wei, T., Schmidt, R. & McMurtry, P., 2005, Comment on the Clauser chart method for determining the friction velocity, *Exp. in Fluids*, **38**, 695-699.

[52] Wilby, J. F., 1996, Aircraft interior noise, *J. Sound Vib.*, **190**(3), 545-564.